



# Utilization of greenhouse gases through carbon dioxide reforming of methane over Ni–Co/MgO–ZrO<sub>2</sub>: Preparation, characterization and activity studies

Mun-Sing Fan, Ahmad Zuhairi Abdullah, Subhash Bhatia\*

School of Chemical Engineering, Engineering Campus, Universiti Sains Malaysia, Seri Ampangan, 14300 Nibong Tebal, Pulau Pinang, Malaysia

## ARTICLE INFO

### Article history:

Received 5 May 2010

Received in revised form 19 July 2010

Accepted 10 August 2010

Available online 14 August 2010

### Keywords:

Nickel–cobalt catalyst

MgO–ZrO<sub>2</sub> support

Carbon dioxide reforming

Methane

Syngas

## ABSTRACT

MgO–ZrO<sub>2</sub> mesoporous support (Zr/Mg molar ratio = 9) impregnated with 6 wt% Ni, 6 wt% Co and 3 wt% of both Ni and Co were prepared using a novel surfactant assisted-impregnation method. Carbon dioxide reforming of methane using these catalysts was studied in a quartz tube microreactor at a CH<sub>4</sub>/CO<sub>2</sub> feed ratio of 1, 750 °C, 1 atm with a gas hourly space velocity of 125,000 mL/g/h. Based on reactant's conversion and syngas production, the bimetallic catalyst was the most suitable catalyst for the reaction. The catalyst exhibited high and constant activity during 40 h reaction time with methane and carbon dioxide conversions of 80% and 84%, respectively with a syngas ratio close to unity without significant deactivation as compared to the respective monometallic catalysts. For longer time on stream, the catalyst showed constant activity up to 60 h after which it gradually decreased. The bimetallic catalyst also exhibited excellent regenerability by restoring its initial catalytic activity after 1 h of regeneration in air. The catalysts were also characterized by XRD, XPS, N<sub>2</sub>-physisorption, H<sub>2</sub>-chemisorption, TGA-DTA, HRTEM, H<sub>2</sub>-TPR, TPH and SEM. The high performance of the bimetallic catalyst was due to the stabilization of t-phase in zirconia, better metal dispersion, small metal particle size and synergetic effect between Ni and Co particles. The XPS results showed that bimetallic catalyst had the ability to hinder metal oxidation and exhibited presence of higher surface basicity which were responsible to maintain the stability of the catalyst.

© 2010 Elsevier B.V. All rights reserved.

## 1. Introduction

Syngas, a mixture of H<sub>2</sub> and CO, is an important feedstock in the production of petrochemicals [1]. It plays the role as an intermediate to convert natural gas to liquid fuel via Fischer-Tropsch synthesis [2]. Commonly, syngas is produced by steam reforming (CH<sub>4</sub> + H<sub>2</sub>O → CO + 3H<sub>2</sub>) and partial oxidation of methane (CH<sub>4</sub> + 0.5O<sub>2</sub> → CO + 2H<sub>2</sub>). In methane steam reforming process, CO<sub>2</sub> is also produced along with the syngas. The separation of CO<sub>2</sub> and its disposal are major issues in petrochemical industry [3]. Meanwhile, steam reforming of methane is mostly applicable to ammonia industry and is a highly endothermic process [4] and produces syngas with a H<sub>2</sub>/CO ratio ≥ 3. Partial oxidation of methane (POM) to syngas is reported as a mildly exothermic process to make syngas and advantageous over the conventional steam reforming of methane [5].

Lately, carbon dioxide reforming (CH<sub>4</sub> + CO<sub>2</sub> → 2CO + 2H<sub>2</sub>) gained research interest for syngas production [6] and as chemical energy transmission system [7]. This process produces unity ratio of syngas, which can be preferentially used for the production of

Fischer-Tropsch liquid hydrocarbon and oxygenates [8]. The most important advantage to be offered by carbon dioxide reforming is the utilization of undesired greenhouse gases (CO<sub>2</sub> and CH<sub>4</sub>). Carbon dioxide reforming of methane will be a potential process for the production of syngas in the future along with steam reforming and partial oxidation reforming process.

However, commercialization of carbon dioxide reforming technology remains a great challenge as it suffers from severe catalyst deactivation through coke deposition. The problem originates from methane decomposition (CH<sub>4</sub> → C + 2H<sub>2</sub>) and Boudouard reaction (2CO → C + CO<sub>2</sub>). Different types of supported metal catalysts have been extensively studied to minimize coke deposition problem. Generally, carbon dioxide reforming is catalyzed by two main groups of catalyst, i.e. nickel (Ni) based catalysts [9,10] and noble metal catalysts [11]. The former group is more favorite from an industrial standpoint due to low cost [12]. However, Ni based catalysts suffer from significant coke formation, sintering effect that is caused by high reaction temperature and metal oxidation to restrain its practical application in industry.

Bimetallic catalyst system with respect to active surface elements can provide few advantages for carbon dioxide reforming of methane. Liu et al. [13] studied a series of catalyst modifiers, i.e. titanium (Ti), manganese (Mn) and zirconium (Zr) incorporated into Ni-based catalysts and found that Ni–Zr bimetallic catalyst exhib-

\* Corresponding author. Tel.: +60 4 5996409, fax: +60 4 5941013.

E-mail address: [chbhatia@eng.usm.my](mailto:chbhatia@eng.usm.my) (S. Bhatia).

ited higher catalytic activity and better stability compared to the other two catalysts. It was attributed to strong anchoring effects of  $Zr^{4+}$  and partial activation of  $CO_2$  by  $Zr^{4+}$ . Besides those mentioned modifiers, cobalt (Co) has attracted recent interest as the second metal to be doped with nickel to form bimetallic catalyst [9,14,15]. Zhang et al. [16] reported that bimetallic catalyst of Co–Ni had great tolerance to coke formation due to the synergetic effects, highly dispersed active metal and strong metal–support interactions. Similar bimetallic catalyst systems were also studied by other researchers and they found that the particle size of catalyst significantly affected the long term conversion of reactants [15].

Many researchers have addressed the issue of coke deposition in Ni-based catalysts, by choosing different types of support. These include basic supports such as alkali or alkaline earth metal oxides that could possibly reduce coke formation [17,18]. Generally, the interest in zirconia ( $ZrO_2$ ) [19–24] as a support material can be attributed to: (1) it contributes to a metal support interaction between the active metal site and support influencing the catalytic activity and selectivity of desired product and, (2) it possesses acidity or basicity as well as reducing and oxidizing abilities.  $ZrO_2$  exhibits different structural polymorphs that are applicable in catalysis, namely monoclinic, tetragonal and cubic phases [25]. In reforming process, tetragonal phase (t-phase) is more desirable compared to monoclinic and cubic phases [26,27]. However, pure  $ZrO_2$  is not stable in the tetragonal phase at room temperature.

It has been reported that t-phase, a desired phase for reforming process can be synthesized by solid-state reaction, co-precipitation, metal alkoxides hydrolysis, hydrothermal and polymer complex methods with relatively low temperature treatment and no phase transformation occurs [28]. On the other hand, addition of aliovalent oxide dopants such as CaO and  $Y_2O_3$  which form solid solution with  $ZrO_2$  could stabilize the tetragonal phase [25]. Among those aliovalent oxides that can be doped into zirconia, magnesium oxide (MgO) is the most potential ones [29–32]. MgO is distinctive in its basicity (isoelectric point of about 12) and forms a class apart from other supports that exhibit acidic, neutral or amphoteric characteristics [33]. Recently, researchers studied the performance of Ni based catalyst supported on MgO– $ZrO_2$ . Li et al. [34] claimed that modification of  $ZrO_2$  with MgO significantly improved the dispersion of surface active element and promoted the  $CO_2$  conversion during carbon dioxide reforming. Recent literature data showed that this modified support system exhibited stable catalytic performance without significant deactivation, but the conversions for both reactants ( $CH_4$  and  $CO_2$ ) were considerably low [35].

To the best of our knowledge, there are no extensive studies on bimetallic active elements supported on the potential binary support, namely MgO– $ZrO_2$ . The objectives of the present study are focused on: (1) the synergy of bimetallic Ni–Co active sites that may show better catalytic performance than monometallic Ni and Co catalysts; (2) the addition of basic MgO that may improve the stability of t-phase zirconia; (3) the effect or interaction of binary support (MgO– $ZrO_2$ ) with metal active site that present in the bimetallic Ni–Co catalyst, and (4) preparation method of the support to result in nanocrystalline structure and stabilization of t-phase present in zirconia. This structure may enhance the metal dispersion on the surface and consequently catalytic activity. In order to address all those topics, comprehensive characterization tests and catalytic activity studies are needed.

In this work, Ni based catalyst by doping with a second element (Co) and supported on a  $ZrO_2$ –MgO support has been prepared using a surfactant assisted-impregnation method. An annealing process at  $800^\circ C$  has been investigated and further stabilization of the catalyst by nanocrystalline MgO has been attempted. Incipient wetness impregnation method was used to prepare tetragonal  $ZrO_2$  by adding pre-prepared nanocrystalline MgO stabilizer. The activity of the bimetallic catalyst for carbon dioxide reforming of

methane is compared with that of monometallic catalysts. Characteristics of all catalyst developed were obtained using different techniques including XRD, BET, HRTEM, SEM, TPR, TPH, XPS, as well as TGA/DTA. The catalytic performance is correlated with the structural and morphological properties of the catalysts. Finally, effects of several regeneration treatments with hydrogen, nitrogen and air on catalyst stability and carbon formation have also been thoroughly investigated.

## 2. Experimental

### 2.1. Catalysts preparation

The catalysts were prepared via 2 stages of calcinations treatment. Firstly, the support was prepared by incipient wetness technique of  $ZrO(NO_3)_2 \cdot 6H_2O$  on MgO powder. Prior to the impregnation process, the MgO powder was prepared following the reported method [36]. Aqueous solution of  $ZrO(NO_3)_2 \cdot 6H_2O$  (Sigma-Aldrich) at an appropriate concentration to obtain  $ZrO_2$ /MgO ratio of 9:1 was mixed with MgO powder. After impregnation, the product was dried at  $110^\circ C$  for 24 h and calcined at  $800^\circ C$  for 3 h. The second stage of the catalyst preparation was the impregnation of active metal on the prepared support. Monometallic (6 wt% of nickel salt or 6 wt% of cobalt salt) and bimetallic (3 wt% of nickel salt and 3 wt% of cobalt salt) aqueous solutions were impregnated onto the support by keeping the total metal loading at 6 wt%. The final products were dried at  $110^\circ C$  for 24 h in an oven before calcination at  $800^\circ C$  for 3 h. Throughout this manuscript, the monometallic Ni and Co, and bimetallic Ni–Co catalysts are designated as NMZ, CMZ, and NCMZ, respectively where MZ represents the support.

### 2.2. Catalysts characterizations

#### 2.2.1. X-ray diffraction

Structural analysis of the prepared catalysts was performed by X-ray diffraction (XRD) using a Siemens D5000 X-ray diffractometer with  $Cu K\alpha$  radiation operated at 40 kV and 40 mA in a diffraction range of  $2\theta = 20$ – $90^\circ$  and a sweep rate of  $0.04^\circ/s$ .

#### 2.2.2. $N_2$ adsorption–desorption

The specific surface area, average pore diameter and pore volume of the catalysts were analyzed using  $N_2$  adsorption–desorption isotherm in an Autosorb-1-MP instrument (Quantachrome, USA). Prior to the measurements, samples were pretreated in vacuum at  $200^\circ C$  for at least 3 h. The specific surface area was determined from the linear part of the Brunauer–Emmett–Teller (B.E.T.) plot in a relative pressure range ( $P/P_0$ ). The total pore volume was estimated from the amount of gas adsorbed at a relative pressure  $P/P_0$  of 0.99. The Barret–Joyner–Halenda (B.J.H.) pore size distribution was determined from the desorption branch of the isotherm.

#### 2.2.3. High Resolution Transmission Electron Microscopy (HRTEM)

The morphology and particle size distribution of catalyst were determined through High Resolution Transmission Electron Microscope (HRTEM) (Philips TECNAI 20) operated at 200 kV. The samples were prepared by isopropanol dispersion and transfer onto a 3 mm diameter and 400 mesh carbon coated copper grid.

#### 2.2.4. $H_2$ -chemisorption

The total metal dispersion and particle size measurements were obtained using  $H_2$  chemisorption analysis. Prior to the chemisorption, the sample was treated as follows: (1) evacuating the sample for 30 min at  $120^\circ C$ . (2) reducing the sample again at  $450^\circ C$  for 30 min using  $H_2$  and (3) evacuating the sample for another 30 min at

120 °C [14]. Finally, H<sub>2</sub>-chemisorption was carried out at 40 °C in a Micromeritic AutoChem II-2920 system. The total metal dispersion of Co or Ni metal was calculated from the Eq. (1) [37].

$$D_M(\%) = 100 \times \left( \frac{V_S \times SF}{SW \times 22414} \right) \times MW \quad (1)$$

where  $D_M$ : metal dispersion (%);  $V_S$ : Volume of active gas chemisorbed (cm<sup>3</sup> at STP); SF: Stoichiometry factor; SW: Sample weight (g); MW: Molecular weight of active metal (g/mole).

By assuming spherical particles, the particles size of cobalt ( $d_{Co}$ ) and nickel ( $d_{Ni}$ ) as well as the bimetallic Ni–Co component were calculated from  $D_M$  using Eqs. (2)–(4) respectively [38]:

Monometallic catalyst:

$$d(Co) \text{ (nm)} = \frac{96}{D_M(\%)} \quad (2)$$

$$d(Ni) \text{ (nm)} = \frac{101}{D_M(\%)} \quad (3)$$

Bimetallic catalyst:

$$d(Co-Ni) \text{ (nm)} = \left[ \frac{96}{D_M(Co)} \right] \times \left( \frac{Co\%}{100} \right) + \left[ \frac{101}{D_M(Ni)} \right] \times \left( \frac{Ni\%}{100} \right) \quad (4)$$

#### 2.2.5. H<sub>2</sub>-temperature programmed reduction

The reducibility of mono- and bimetallic catalysts were analyzed using temperature programmed reduction (TPR). The study was performed in a Micromeritic AutoChem II-2920 automated system. Sample weight of about 0.5 g was placed in a U-shape quartz tube in a temperature-controlled oven and connected to a thermal conductivity detector (TCD). The catalyst was first purged under 50 cm<sup>3</sup>/min of N<sub>2</sub> flow at 150 °C for 1 h (using a ramp rate of 10 °C/min) and then cooled down to ambient temperature. The reducing gas was 10% H<sub>2</sub> in Argon. During the reduction step, a cold trap was placed before the detector to remove any water produced. The temperature programmed reduction analysis was performed with a constant heating rate of 10 °C/min from 35 to 1000 °C. The amount of hydrogen consumption was measured using a thermal conductivity detector.

#### 2.2.6. X-ray photoelectron spectroscopy (XPS)

X-ray photoelectron spectroscopy (XPS) was used for surface analysis and metal oxidation state investigation using an Omicron Multiprobe spectrometer, using Al X-ray source (Omicron NanoTechnology) available at AMREC, Malaysia. The charging effect was corrected by adjusting the C 1s peak to a position of 284.5 eV. The sample was pressed into disc and mounted on a sample rod in a pretreatment chamber. The spectrum of Ni 2p, Co 2p and O 1s was recorded.

#### 2.2.7. Thermogravimetry/differential thermal analysis

Thermogravimetric (TG) analysis was conducted to study the amount of coke deposited on used catalysts. The thermal analysis was carried out in pure O<sub>2</sub> flow (50 mL/min) with TGA/DSC instrument (METTLER TOLEDO). Used catalyst (8–10 mg) was heated from ambient temperature to 800 °C at 10 °C/min. The amount of deposited carbon was determined from weight loss by using STARE software incorporated in the TGA/DSC instrument.

#### 2.2.8. Temperature programmed hydrogenation (TPH)

Temperature programmed hydrogenation of used catalyst was conducted following the method reported in literature [6,39,40]. TPH was performed to characterize carbon species present on the catalyst formed during catalytic reforming reaction. The used catalyst was outgassed under inert atmosphere, at 150 °C for 1 h before subject to heat treatment (10 °C/min up to 1000 °C) in a gas mixture

10% H<sub>2</sub> in Argon with flowrate of 50 mL/min. The vent gas was analyzed with a thermal conductivity detector (TCD). A cold isopropyl alcohol–liquid nitrogen (IPA/LN<sub>2</sub>) slurry trap was set between the sample cell and detector to condense the produced moisture.

#### 2.2.9. Scanning electron microscope (SEM)

The morphology of coke deposited on the spent catalyst after long term activity was determined using a Zeiss (Oberkochen, Germany) Supra 35 VP scanning electron microscope (SEM) with W-tungsten filament, operated at 3.00 kV.

### 2.3. Catalytic activity study

The catalytic activities were studied in a fixed-bed continuous-flow reactor. The experimental setup consists of 3 sections: Gases delivery, catalytic reactor and products analysis as shown in Fig. 1. Methane (CH<sub>4</sub>, 99.95%), carbon dioxide (CO<sub>2</sub>, 99.95%) and nitrogen (N<sub>2</sub>, 99.99%) were used to form the synthetic mixture of feed gas. The catalytic reactor made of quartz with 10 mm internal diameter and 40 cm length was mounted vertically inside a tubular furnace. A Type-K thermocouple was placed into the annular space between the reactor and tubular furnace to measure the reactor temperature while the second thermocouple of same type was placed in the middle of the catalytic reactor bed in order to measure the actual temperature of the bed inside the reactor [41]. The quartz tube reactor was charged with 0.1 g of calcined catalyst and sandwiched by quartz wool layers to maintain the bed at the desired location. The post catalytic volume was filled up with quartz wool to reduce the free volume and to diminish further reaction of the desired products (syngas) to undesired products (H<sub>2</sub>O and CO<sub>2</sub>) [42]. The reaction conditions were: an equimolar gas mixture of methane, carbon dioxide and nitrogen, 750 °C, 0.1 g of catalyst (0.15–0.18 mm), and a gas hourly space velocity (GHSV) of 125,000 mL/g/h. All catalysts were reduced *in situ* for 3 h in 90% hydrogen/10% nitrogen at a flow rate of 30 mL/min before the catalytic activity tests were performed. The reaction products were analyzed using an online gas chromatograph (GC, Agilent 6890N) integrated with Agilent ChemStation software. The gaseous product was sent into the GC for analysis with argon as the carrier gas. The temperature setting inside the GC column was programmed varying with time. In the first 0.1 min, the oven temperature was constant at 100 °C, it was then decreased steadily by the rate of 10 °C/min until 65 °C. Finally, the temperature was increased to 10 °C and hold for 13.5 min. Two different columns i.e. Porapak Q column for the separation of CH<sub>4</sub>, and a 0.5 nm molecular sieve column for the separation of H<sub>2</sub>, CO<sub>2</sub>, N<sub>2</sub>, and CO were used. The conversions of reactants and syngas ratio are defined as follows:

$$\text{Conversion of CH}_4, X_{CH_4}(\%) = \left( \frac{F_{CH_4, in} - F_{CH_4, out}}{F_{CH_4, in}} \right) \times 100 \quad (5)$$

$$\text{Conversion of CO}_2, X_{CO_2}(\%) = \frac{F_{CO_2, in} - F_{CO_2, out}}{F_{CO_2, in}} \times 100 \quad (6)$$

$$\text{Selectivity of H}_2, S_{H_2} = \frac{F_{H_2, out}}{2(F_{CH_4, in} - F_{CH_4, out})} \times 100 \quad (7)$$

$$\text{Selectivity of CO}, S_{CO} = \frac{F_{CO_2, out}}{[(F_{CH_4, in} - F_{CH_4, out}) + (F_{CO_2, in} - F_{CO_2, out})]} \times 100 \quad (8)$$

$$\text{Ratio of H}_2/\text{CO} = \frac{\text{selectivity of H}_2}{\text{selectivity of CO}} \quad (9)$$

$$F_{i, in/out} = F_{total} \times C_i$$

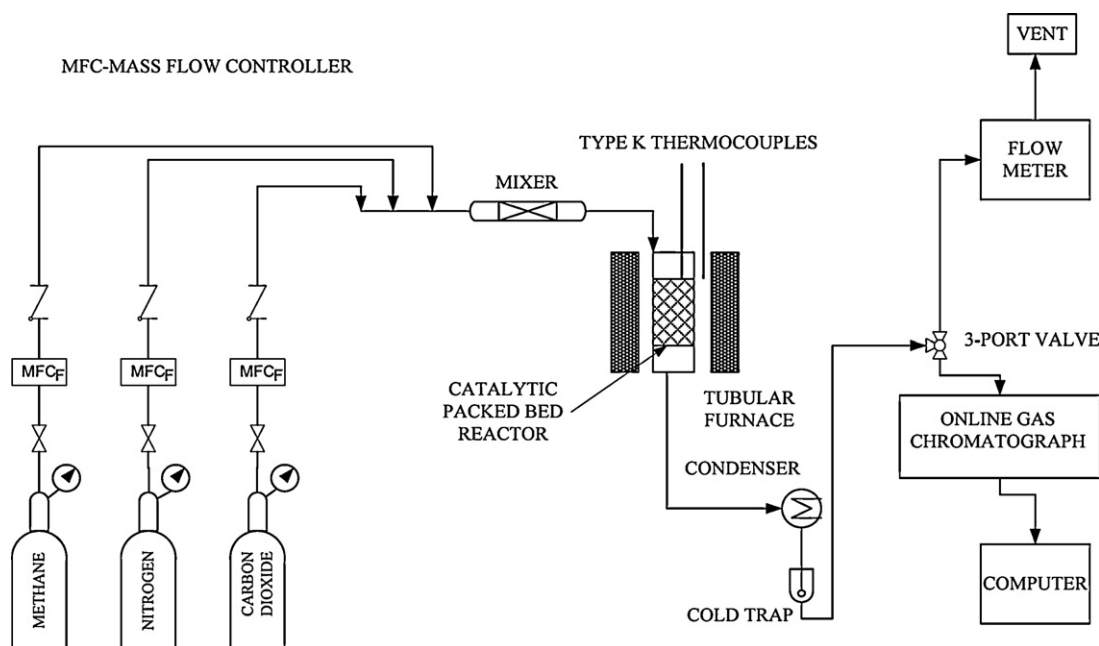


Fig. 1. Experimental setup for carbon dioxide reforming of methane.

where  $F_{i,\text{in/out}}$  is the flow rate of each component in the feed or effluent,  $F_{\text{total}}$  represents the total flow rate of gaseous products, and  $C_i$  is the molar fraction of component  $i$  in the gaseous effluent.

### 3. Results and discussion

#### 3.1. XRD analysis

Structural properties of supported catalysts were investigated using XRD method. The XRD patterns of the catalysts are presented in Fig. 2. It was noted that bimetallic catalyst was well crystallized under the calcination condition (800 °C). Monometallic catalysts showed relatively boarder peaks (amorphous). Generally,  $\text{ZrO}_2$  can have three kinds of crystallographic forms based on the annealing temperature [43]: at room temperature, pure  $\text{ZrO}_2$  occurs in the monoclinic phase changing to tetragonal phase at 1170 °C. At temperature close to 2370 °C, tetragonal phase  $\text{ZrO}_2$  crystallizes as cubic phase and it melts at 2680 °C [43,44]. It has been reported that, cubic and monoclinic phases gave lower catalytic activity compared to the tetragonal phase [45]. Tetragonal phase zirconia (t- $\text{ZrO}_2$ ) is

considered as the desired phase which exhibits both acidic and basic properties [46], and active in many heterogeneous catalytic systems [18,47]. From the XRD patterns of all synthesized catalysts, the support was dominated by t- $\text{ZrO}_2$  identified with peaks at  $30.05^\circ$  (1 0 1),  $34.20^\circ$  (1 1 0),  $50.05^\circ$  (1 1 2) and  $59.85^\circ$  (2 1 1). No significant peaks for monoclinic phase zirconia were detected among those synthesized catalysts as compared to the XRD pattern for monoclinic zirconia as reported by García et al. [35].

Stabilization of t- $\text{ZrO}_2$  on the support was associated with the presence of MgO [48] and its size effect [49]. The addition of MgO to  $\text{ZrO}_2$  support inhibited sintering effects between the crystallites of t- $\text{ZrO}_2$  and prevented the transformation of zirconia support from tetragonal phase to monoclinic phase [48]. Rezaei et al. [49] proposed that through certain surfactant-aided preparation method, nano-size effect of the zirconia could lead to the thermal stabilization of t-phase. In current work, no apparent peaks of  $\text{CoO}$  and  $\text{Co}_2\text{O}_3$  were identified in the XRD analysis for cobalt supported and bimetallic catalysts. This was probably due to the high dispersion of cobalt. Specifically in the bimetallic catalyst, spinel type solid solution of  $\text{NiCo}_2\text{O}_4$  was detected. The formation of spinel phase for the two active metals could be due to high temperature treatment during calcinations [50].

XRD result shows the formation spinel like solid solution compounds of  $\text{Ni}_x\text{Mg}_{1-x}\text{O}$  and  $\text{Co}_x\text{Mg}_{1-x}\text{O}$  in bimetallic catalyst samples. These were difficult to be distinguished due to the similar morphology and characteristic peaks [51]. It can be seen from the XRD result that peak overlapping occurred for  $\text{NiO}$  and  $\text{Ni}_x\text{Mg}_{1-x}\text{O}$  due to similar reflection angles and intensities. It can be concluded that spinel type solid solutions were present in the catalysts due to formation of spinel type active structure during the heat treatment.

#### 3.2. $\text{N}_2$ -adsorption/desorption isotherm analysis

Nitrogen adsorption analyses were conducted in order to obtain the surface area and pore size distribution of different catalysts. Sorption isotherm curves of all the catalysts and support samples showed a similar pattern in Fig. 3. A sharp inclination of nitrogen uptake at  $P/P_0 > 0.9$  with a hysteresis loop was identified for all catalysts and was categorized as type II isotherm. Type II isotherm is very common in physical adsorption cases in porous materi-

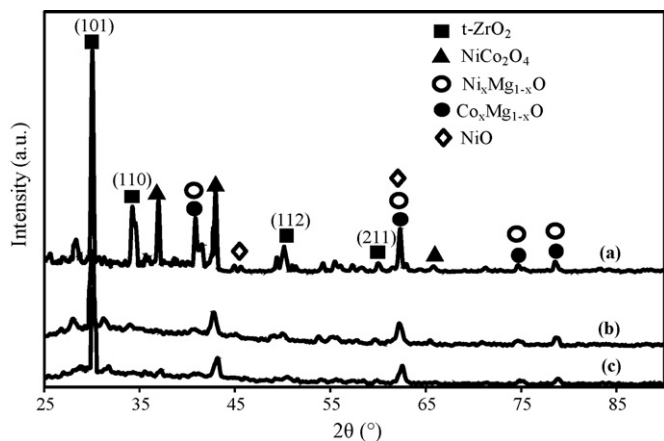


Fig. 2. XRD patterns of Ni or/and Co supported on  $\text{MgO-ZrO}_2$  catalysts. (a) NCMZ; (b) NMZ; (c) CMZ.



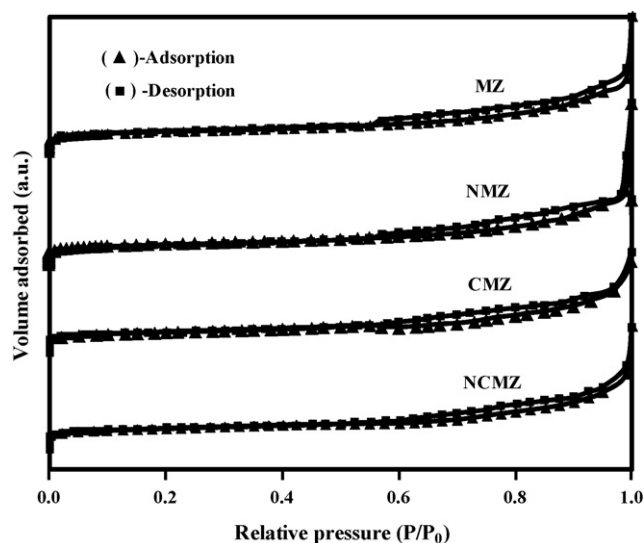


Fig. 3. N<sub>2</sub> adsorption/desorption isotherms for the support and metal catalysts.

**Table 1**  
Structural properties of the catalysts and support.

Sample	BET area (m <sup>2</sup> /g)	Pore Volume (cm <sup>3</sup> /g)	Pore diameter (nm)
NCMZ (■)	148.5	0.351	3.20
CMZ (◆)	150.2	0.364	3.38
NMZ (▲)	155.8	0.371	3.42
MZ (●)	169.8	0.431	4.22

als and corresponds to multilayer formation [52,53]. These results show that the catalysts contained slit-shaped pores or aggregates of platy particles [54] with narrow pore size distribution as shown in Fig. 4 (0.81–10.5 nm). Fig. 3 shows the adsorption type II which belongs to microporous structure type of hysteresis [55]. However, Fig. 4 shows the average pore size distribution fall between micropores (<2 nm) and mesopores (>2 nm and <50 nm) range. Thus, both mesopores and micropores were present in all the catalysts. The microporous and mesoporous structures played an important role in the metallic catalyst, to avoid the sintering of surface metal particles through the “confined effect” which limited the growth of metal crystallites during high temperature reaction [56].

The results of textural examination are tabulated in Table 1. The incorporation of active components (Ni and/or Co) on MZ support caused reduction in the specific surface area, pore volume and pore diameter as compared to those of the support. A drop in the surface area could be due to the deposition of metal particle inside

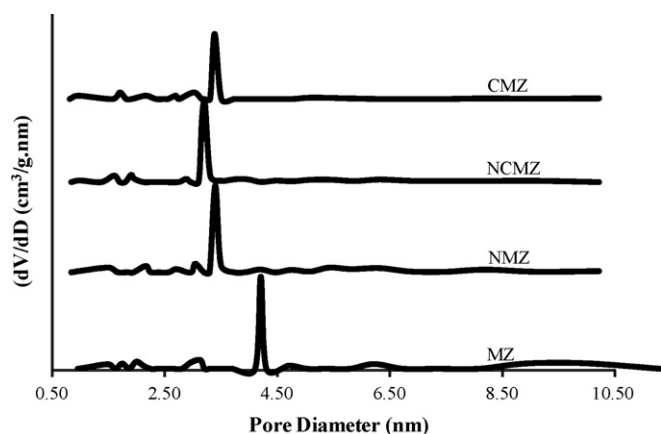


Fig. 4. Pore size distribution of support and catalysts.

the pores of support or partial blockage of pores [57]. The bimetallic NCMZ catalyst experienced high reduction as compared to the MZ support. This could be attributed to the partial substitution of bimetallic particles in the pores. However, both monometallic catalysts, i.e. CMZ and NMZ showed comparable values to those of NCMZ catalyst. These results showed that the monometallic particles are mostly presented on the external surface of support instead of the internal surface (NCMZ catalyst).

Fig. 4 shows pore size distributions of all freshly calcined catalysts. It is noted that the catalyst samples and support had narrow pore size distribution ranging from 0.81 to 10.5 nm. The support also exhibited presence of nano-size pores which were in agreement with the XRD results to suggest that the nano-size effect could stabilize the t-phase of zirconia. The narrow pore size distribution exhibited by all catalyst samples showed better metal dispersion for monometallic as well as bimetallic catalysts.

### 3.3. Metal dispersion and particle size distribution

Metal particle morphology and particle size distribution of the catalysts were investigated using HRTEM. Fig. 5 shows the HRTEM images, SAED diffractograms and particle size distribution curve for each of the catalyst. From the HRTEM images, support material for all samples exhibited mesoporous structure with a plate-like shape. Different morphology of MgO–ZrO<sub>2</sub>, in which, the support exhibited a sponge-like mesoporous network has been reported in the literature [58]. This discrepancy could result from the different preparation methods used in the present study. It is interesting to note that metal particles were distributed uniformly from each other and there was no significant agglomeration of metals detected.

On the basis of SAED diffractogram, bimetallic catalyst was polycrystalline and made up of the formation of clear concentric rings derived from an assembly of nanocrystallites [36]. On the other hand, CMZ and NMZ catalysts showed the presence of a mixture of polycrystalline and amorphous phase. These observations were in agreement with XRD patterns, revealing that the bimetallic catalyst showed higher crystallinity compared to the monometallic catalysts. The metal particle size for all catalysts was estimated by computing the size of 150 particles. The largest particle was obtained for CMZ (6.25 nm) catalyst followed by NMZ (5 nm) catalysts. NCMZ catalyst showed the smallest particle size (3.1 nm). When the amount of metal loading in bimetallic catalyst was reduced to half of the original metal loading in monometallic catalyst, significant size reduction (≈50% reduction) was noticed. This observation could be possibly caused by strong metal support interactions for bimetallic catalyst towards binary support [16].

Metal dispersion,  $D_M$  was calculated with the assumption that all metals (spherical particles) were present on the surface [59]. By using HRTEM images [16], the following equation was used to calculate metal dispersion [59].

$$D_M = 6 \times 10^8 \left( \frac{V_M}{A_M} \right) \frac{1}{d} \quad (10)$$

where  $V_M$  is the bulk atomic volume of the metals (cm<sup>3</sup>),  $A_M$  is the area of an atom (cm<sup>2</sup>), and  $d$  is the average metal particle size in nm estimated from HRTEM images.  $1.10 \times 10^{-23}$  cm<sup>3</sup> is taken as the value of  $V_M$  for both Ni and Co as they are very close to each other in periodic table [16]. Yu and Oyama [60] reported the value of  $A_M$  was estimated to be  $1 \times 10^{-15}$  cm<sup>2</sup>. The calculated metal dispersion results are presented in Table 2. In general, bimetallic catalyst (with smallest particle size) showed higher metal dispersion compared to the larger particle size monometallic catalyst. It has been reported in literature that [14], the synergy between the bimetallic elements could enhance the metal dispersion on the support material.

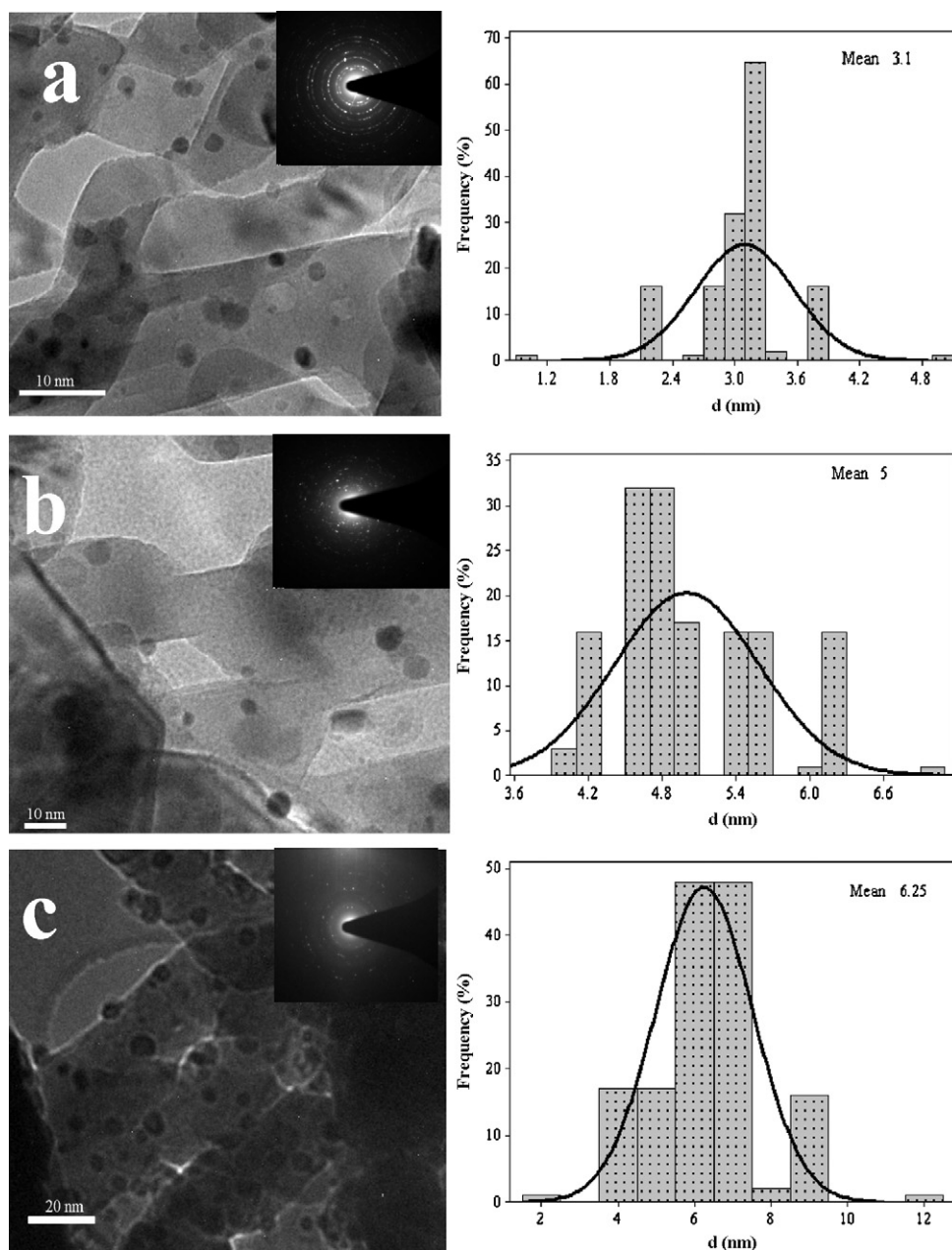


Fig. 5. HRTEM images, SAED diffractograms and particle size distribution of fresh catalysts. (a) NCMZ, (b) NMZ, (c) CMZ.

The metal particle size and dispersion were further investigated through  $H_2$ -chemisorption at 40 °C, assuming that the chemisorption stoichiometry of H/metal was equal to 1 [49]. Table 2 also presents the amount of  $H_2$  adsorbed ( $cm^3$  STP), corresponded to the number of active metals reachable to the reactants molecules. Generally, metal dispersion as determined by  $H_2$ -chemisorption technique gave higher value but the same order of magnitude as calculated from HRTEM images. This discrepancy might be ascribed

to many reasons such as the ratio of H to metal could be less than 1, the hydrogen uptake could be particle size-dependent or small metal particle could be embedded in the support lattices [61]. The bimetallic NCMZ catalyst showed significantly higher metal dispersion compared to CMZ and NMZ catalysts. This observation was due to the formation of spinel like solid solution in monometallic catalyst which could not chemisorb hydrogen at room temperature [62]. Although the catalysts were prepared with a 6 wt% nominal

**Table 2**  
 $H_2$  chemisorption of the catalysts.

Sample	$H_2$ uptake ( $cm^3$ stp)	Metal size from chemisorption (nm)	Metal size of fresh catalyst from HRTEM (nm)	Metal size of used catalyst from HRTEM (nm)	Metal dispersion from $H_2$ uptake (%)	Metal dispersion from HRTEM (%)
NCMZ	2.34	2.00	3.10	3.31	24.6	21.3
NMZ	1.55	6.20	5.00	5.21	16.1	13.2
CMZ	1.28	7.10	6.30	6.87	13.5	10.5

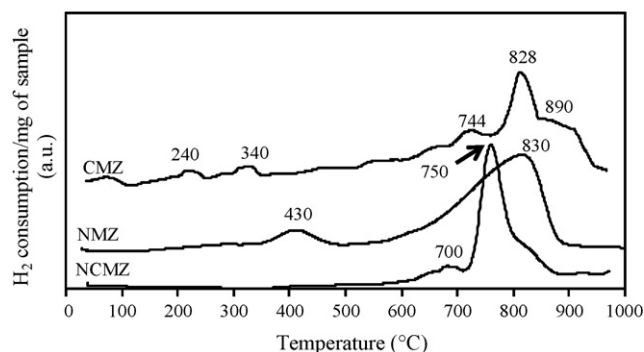


Fig. 6. TPR profiles of monometallic (Ni/Co) and bimetallic (Ni-Co) supported catalysts.

total metal content, bimetallic catalyst showed higher  $H_2$  uptake as well as metal dispersion as compared to both monometallic catalysts. This phenomenon is generally observed in the case of evenly distributed particles and synergized effects of active metals on the support [16].

### 3.4. Temperature programmed reduction

TPR analysis was conducted to unveil the synergy effects between Ni and Co supported on  $MgO-ZrO_2$ . As can be observed in Fig. 6 shows, at lower reduction temperature ( $<400^\circ C$ ), two significant peaks were detected for CMZ catalyst, corresponded to the reduction of  $CoO$  to  $Co_3O_4$  at  $240^\circ C$  and the reduction of  $CoO$  to  $Co$  at  $340^\circ C$  [63,64]. As the reduction temperature was increased, another two main reduction peaks were observed. A peak at  $744^\circ C$  was attributed to the reduction of  $Co-O-Zr$  species [65]. However, according to other researchers that worked on similar catalyst system [66], the reduction of solid solution for  $CoO$  and  $ZrO_2$  was not observed. Instead, only the formation of solid-solid interaction between cobalt particles and  $MgO$  to give  $MgCo_2O_4$  that showed a reduction peak at  $828^\circ C$  was observed. It was noted from the TPR profile that a small reduction peak appeared at  $890^\circ C$ . The formation of this peak could be possibly caused by the complete reduction of  $MgCo_2O_4$  to metallic cobalt. It can be concluded from the TPR result that CMZ catalyst showed strong interaction between  $Co$  particle and nanocrystalline mesoporous supports.

In the case of NMZ catalyst reduction, the lower reduction peak at  $430^\circ C$  could be ascribed to the reduction of  $Ni^{2+}$  in the  $Ni^0$  phase [67]. This low temperature reduction peak could be assigned to the reduction of  $NiO$  species located on the  $MgO$  surface or to the reduction of  $Ni^{2+}$  ions having square-pyramidal organization in the most external layer of the  $MgO$  structure [68]. The second reduction peak at  $830^\circ C$  was attributed to the reduction of  $Ni^{2+}$  seated deep in the  $MgO$  lattice [69]. For the bimetallic NCMZ catalyst, two reduction peaks at  $700$  and  $750^\circ C$  were observed. These peaks appeared at lower reduction temperature than that of the main peaks in both monometallic catalysts and could be possibly caused by the reduction of more dominated spinel-like solid solution species. Thus, it showed the existence of synergized effect between nickel and cobalt during the process of catalyst preparation [67].

It can be seen from the TPR profile that NMZ catalyst exhibited the highest hydrogen consumption. In other words, this catalyst was the hardest to be reduced. The high surface area for NMZ (Table 1), could contribute to more surface oxygen species and consequently reacted with larger amount of hydrogen [70]. Whereas these 3 catalysts were prepared using the same amount of support materials, the effect of support, especially zirconium site was more pronounced for bimetallic NCMZ catalyst. Therefore, the use of zirconium increased the reducibility of surface species due to the

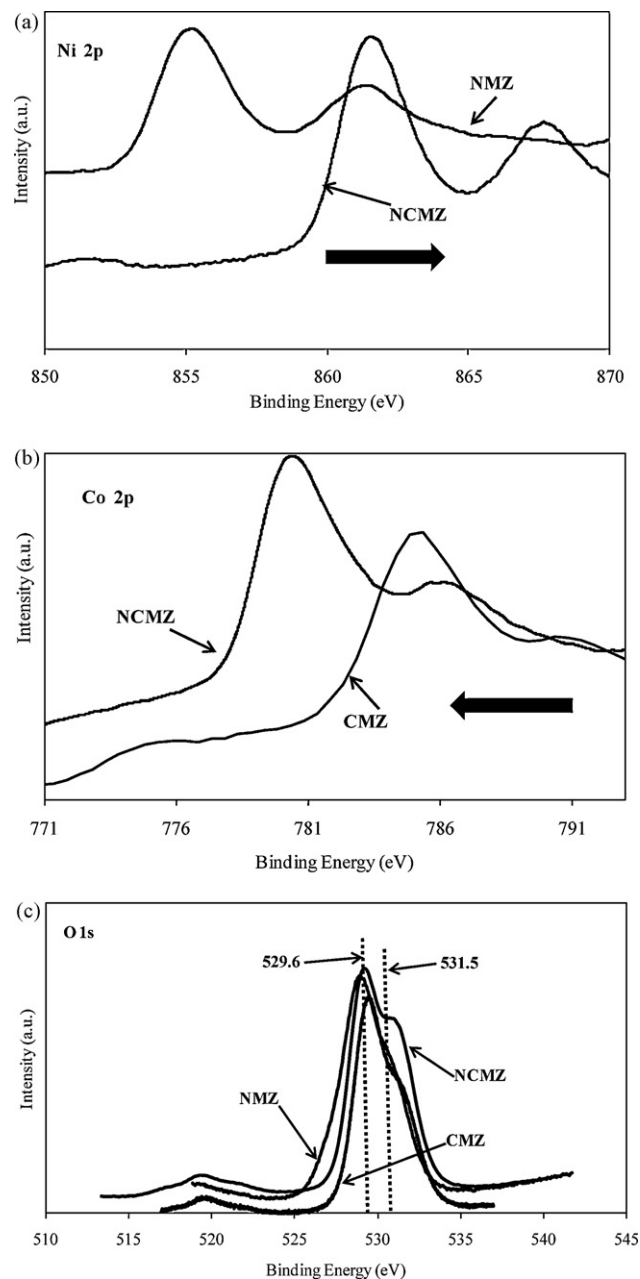


Fig. 7. XPS spectra of (a) Ni 2p, (b) Co 2p, (c) O 1s of the catalysts.

lattice distortions and improved the oxygen mobility on the surface of support [71]. Zirconium played more significant role as a promoter to promote the reducibility in bimetallic catalyst compared to monometallic catalysts and to some extent of metal support interaction that significantly lowered the reduction temperature as shown in Fig. 6.

### 3.5. X-ray photoelectron spectroscopy (XPS)

X-ray photoelectron spectroscopy (XPS) study was conducted for surface and metal oxidation state analyses. Ni 2p and Co 2p spectra of fresh catalysts are shown in Fig. 7a and b, respectively. It can be seen in the figures that significant peaks migration from lower to higher binding energy or vice versa occurred. Fig. 7a shows that NMZ catalyst had a binding energy of  $855.4\text{ eV}$  assigned to the presence of  $Ni^{2+}$  species [72] and shifted to  $861.8\text{ eV}$  in bimetallic catalyst. CMZ catalyst displayed a peak at  $784.8\text{ eV}$ . This peak did not

**Table 3**  
Catalytic activity for carbon dioxide reforming.

Catalyst	Initial conversion (%)		Final conversion (%) <sup>a</sup>		Percent changes in conversion (%)		H <sub>2</sub> /CO Ratio
	CH <sub>4</sub>	CO <sub>2</sub>	CH <sub>4</sub>	CO <sub>2</sub>	CH <sub>4</sub>	CO <sub>2</sub>	
NMZ	75	80	70	73	−6.7	−8.8	0.88
NCMZ	75	80	80	84	6.7	5.0	0.97
CMZ	78	78	71	74	−9.0	−5.1	0.91

<sup>a</sup>40 h of reaction time.

Negative sign (−) indicates the decrease in catalytic activity.

identical with typical Co binding energies (BEs) that normally registered at 779.9 eV as reported in literature [73]. This observation was due to the synchronization of cobalt cations with hydroxyl group due to the chemical shift [74,75]. CMZ catalyst showed a migration of oxidation state from 784.7 eV to a lower oxidation state, at 780 eV for the NCMZ catalyst, assigned as metallic cobalt [72] implying a higher electron density in the Co species in the bimetallic catalyst. Cheekatamarla and Lane [76] reported that electronic compositions and remarkable shifts in the relative binding energies may be caused for alloy formation. However, the formation of alloy in the NCMZ was not proven by other characterizations such as TPR technique where peaks were found instead of one stage reduction that indicated the formation of bimetallic alloy [77]. The impact of these changes in oxidation state may contribute to protect active metal from undergoing further oxidation process at high reaction temperature [14,72].

The surface basicity also can be investigated through XPS study. Cairon et al. [78] investigated the acid-basicity on mixed oxide and found that the main part of the basicity on metal oxide is due to the surface hydroxyl group. The existence of hydroxyl group could be verified based on O 1s spectra. The O 1s signals for all catalysts i.e. CMZ, NMZ and NCMZ are shown in Fig. 7c. The spectra demonstrating a peak between 529.2 and 529.7 eV as well as a shoulder located towards the direction of higher binding energies, approximately at around 531.5 eV. Generally, O 1s spectra could be resolved to two sub spectra according to two BEs locations. The lower BEs of 529.2–529.7 eV were assigned to bulk oxide (O<sup>2−</sup>) and peak at 531.5 eV was registered as hydroxyl species [75]. There is moderate shift of BEs value for the first peak in which the value of 529.2 eV for NMZ catalyst increased to 529.6 eV (dotted line) for NCMZ catalyst. The BEs value for CMZ catalyst shifted to lower value where it dropped from 529.7 to 529.6 eV. The changes in BEs value indicate the shift of oxidation state as explained earlier. It has been reported in the literature that [35,75] hydroxyl and oxygen groups were derived from the oxide support, i.e. MgO.

As mentioned earlier, the surface basicity was due to the hydroxyl group. From Fig. 7c, the intensity of O 1s spectra at 531.5 eV of NCMZ catalyst was significantly higher than both monometallic catalysts, namely NMZ and CMZ catalysts. In the present study, all catalysts were prepared using the same amount of support materials, but the XPS spectra showed different intensities of surface oxygen species. This discrepancy most probably was due to the differences in metal dispersion on the surface. Chary et al. [79] reported that the metal dispersion can be correlated to the intensity of XPS spectra. Metal dispersion as given in Table 2 shows that bimetallic catalyst has higher metal dispersion compared to monometallic catalysts while the metal dispersion of both monometallic catalysts are similar.

### 3.6. Catalytic activity measurement

The catalytic activity of the catalysts was monitored as methane conversion, CO<sub>2</sub> conversion and syngas ratio in the product stream. The conversion and ratio data were obtained by running the catalytic activity experiments continuously against reaction time.

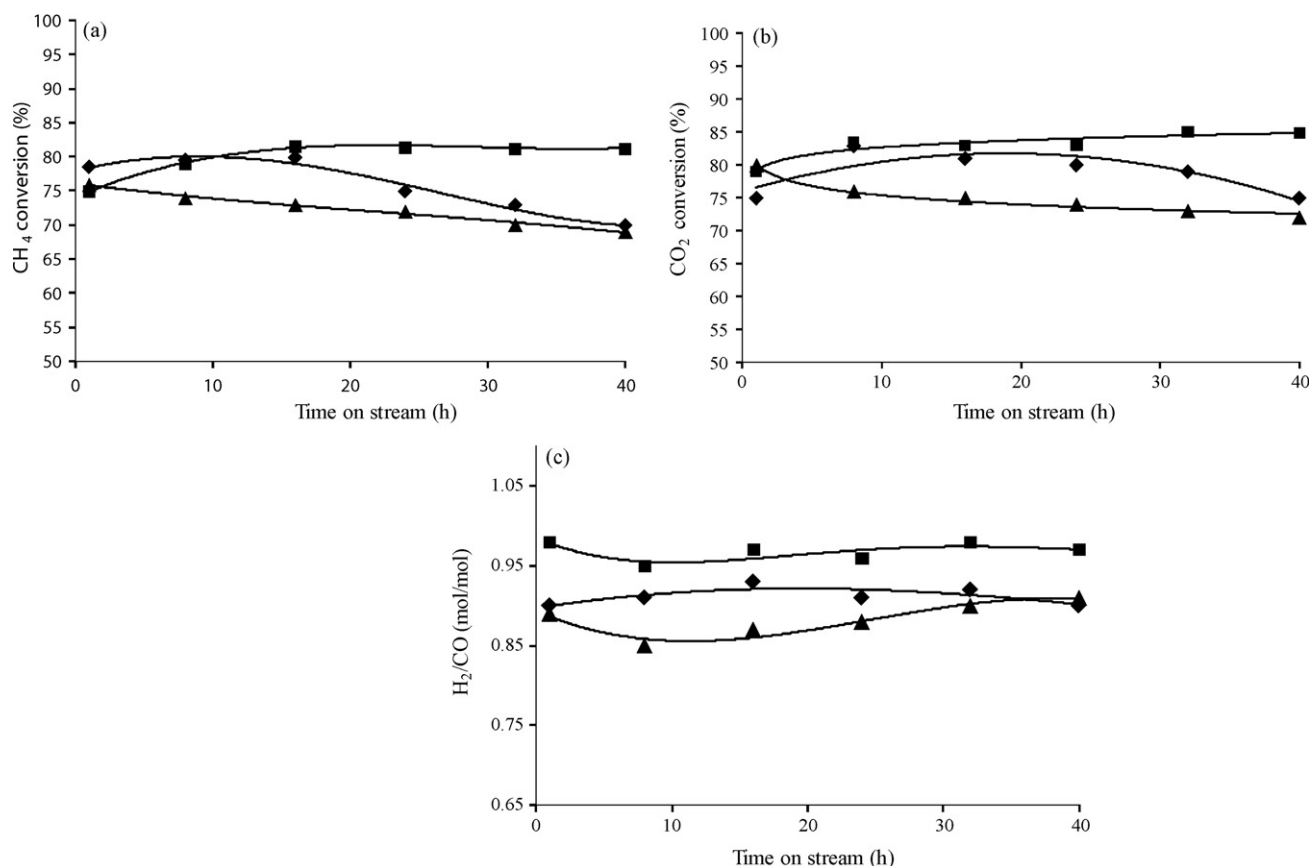
Fig. 8a and b show the conversion profile of methane and carbon dioxide, for all the samples tested at 750 °C as a function of time on stream. The reaction conditions were chosen based on similar catalyst system reported in literature [16]. The high reaction temperatures (750 °C and above) are more favorable thermodynamically, to increase the equilibrium conversion of the carbon dioxide reforming (high endothermic reaction) than those of the side reactions including methane decomposition (CH<sub>4</sub> → C + 2H<sub>2</sub>), the Boudouard reaction (2CO → C + CO<sub>2</sub>) as well as the reversed carbon gasification reaction (CO + H<sub>2</sub> ↔ C + H<sub>2</sub>O) [14,80,81]. These side reactions could contribute to the deactivation of catalyst.

Fig. 8c shows the profile of syngas ratio versus the time on stream. The conversion and syngas ratio data are presented in Table 3. Generally, the conversion of CH<sub>4</sub> was lower than CO<sub>2</sub> conversion. This phenomenon could be attributed to the reverse water gas shift reaction (CO<sub>2</sub> + H<sub>2</sub> → 2CO + H<sub>2</sub>O) taking place during reforming reaction. A small amount of water was found in the cold trap after 40 h of reaction. The reversed water gas shift reaction (RWGS) was also confirmed by the ratio of syngas being less than unity [14]. It was observed that the syngas ratio changed in an oscillating pattern for all studied catalysts, which could be ascribed to the effect of carbon deposition and elimination [27].

From the conversion data, it could be seen that CMZ (◆) catalyst showed high initial activity while NCMZ (■) and NMZ (▲) catalysts showed almost similar initial activity. As per to the TPR results (Fig. 6), the reduction of CMZ was relatively easy as the reduction temperature (<400 °C) was much lower than reaction temperature (750 °C) but most of the particle remained in the form of MgCo<sub>2</sub>O<sub>4</sub> in which catalytically non-active [66] (reduction temperature as high as 828 °C). As a result, the high initial activity of CMZ catalyst was due to the activation of catalyst (CoO to Co<sup>0</sup>) by methane (a reductive agent) and consequently by H<sub>2</sub> and CO in the reforming atmosphere [66]. TPR analysis also revealed that both monometallic catalysts exhibited significant higher reduction temperature (>800 °C) compared to bimetallic catalyst (<800 °C). Under the chosen reaction condition of 750 °C for the reaction temperature, the bimetallic catalyst was reduced while monometallic catalysts were partial reduced as can be seen in Fig. 6. Partially reduced monometallic catalysts will remain most of the metallic active sites in oxide form (after high temperature calcinations) rather than existing in active element like Ni<sup>0</sup> and Co<sup>0</sup>. Both reduced solid solution of cobalt (MgCo<sub>2</sub>O<sub>4</sub>) and nickel (NiO–MgO) were active in enhancing the heterogeneous catalytic activity [9,82,83]. As a result, this phenomenon might lead to the continuous deactivation of monometallic catalysts.

The better performance of bimetallic catalyst in terms of reactant conversion as well as stability (Fig. 8) could be due to the better metal dispersion. Bimetallic catalyst showed small metal particles and high dispersion as confirmed from H<sub>2</sub>-chemisorption results and further supported by HRTEM images. An increase in the activity of bimetallic catalyst was due to the increase in the number of active sites present on the catalytic surface. The support played an important role in the catalytic activity due to metal support interactions [16]. Besides the physical properties that influenced the





**Fig. 8.** Activity of the metal catalysts as a function of time on stream (reaction condition:  $T = 750^\circ\text{C}$ ,  $P = 1\text{ atm}$ ,  $\text{GHSV} = 125,000\text{ ml/g h}$ ,  $\text{CH}_4/\text{CO}_2 = 1$ ). (■) NCMZ, (◆) CMZ, (▲) NMZ; (a) CH<sub>4</sub> conversion, (b) CO<sub>2</sub> conversion, and (c) H<sub>2</sub>/CO in the product.

catalytic activity, chemical property also played a significant role in promoting the catalytic activity. As can be seen from Fig. 8b, the CO<sub>2</sub> conversion increased constantly for bimetallic catalyst compared to the conversion obtained with monometallic catalysts which decrease with time on stream. This observation was due to the higher basicity of NCMZ catalyst compared to monometallic catalysts.

### 3.7. Characterizations of the used catalysts

#### 3.7.1. TGA

From literature studies, the reasons for catalyst deactivation in carbon dioxide reforming are attributed to the sintering of metallic particles and carbon deposition on the catalysts [84]. The rate of coke deposited on the catalysts was evaluated by TGA-DTA analyses and the amount of coke deposited is presented in Table 4. A small amount of coke deposited to indicate low coking rate was observed for NMZ catalyst with a coking rate of  $0.18\text{ mg/g}_{\text{catalyst/h}}$ . This observation was in agreement with catalytic performance in which the conversion was quite low and generated less amount of coke. The monometallic cobalt catalyst (CMZ) showed the highest coking rate ( $1.25\text{ mg/g}_{\text{catalyst/h}}$ ) but it did not give high catalytic activity. This result showed that the Co based catalyst generated more carbon

deposits than Ni based catalyst [15]. However, contrary result has been reported by other researchers [9] where monometallic Co catalyst showed lower catalytic activity compared to monometallic Ni based catalyst due to the formation of non-active Co particle. In the present work, bimetallic catalyst showed highest catalytic activity and exhibited moderate coke formation rate of  $0.89\text{ mg/g}_{\text{catalyst/h}}$ . This result indicated that the formation of coke was inevitable and deposited carbon could improve the activity of bimetallic catalyst to some extent.

#### 3.7.2. TEM

In order to investigate on the type of carbon deposited, TEM mapping was conducted and the images are presented in Fig. 9a–c. As it can be seen from the TEM micrographs (pointed areas), all catalysts were covered with coke in the form of filamentous whiskers type. The average size of the deposited coke was around 15 nm in diameter with a hollow core. The metallic crystalline could be encapsulated or remained on the surface of the filamentous carbon. Fig. 10a and c shows metal crystalline (black point) to stay on the surface of filamentous carbon. The filamentous carbon was formed via deposition on the back of metal crystalline [85]. On the other hand, metal crystalline of NMZ catalyst is found to be encapsulated by filamentous coke as shown in Fig. 9b. San-José-Alonso et al. [15] reported that the activity of carbon dioxide reforming was closely related to the type of coke deposited. Severe deactivation occurred on coke encapsulated metal crystalline as a result of the limited accessibility of reactants on metallic active sites while the deposition of coke on the backside of metal crystallites and this caused the reforming activity stable due to the high accessibility of gas phase reactants on metal active sites. In present work, the low activity of NMZ catalyst as shown in Fig. 8a and b could possibly

**Table 4**  
Catalytic activity for carbon dioxide reforming with 40 h time on stream.

Catalyst	Carbon Deposition ( $\text{mg/g}_{\text{catalyst/h}}$ )
NMZ	0.18
NCMZ	0.89
CMZ	1.25

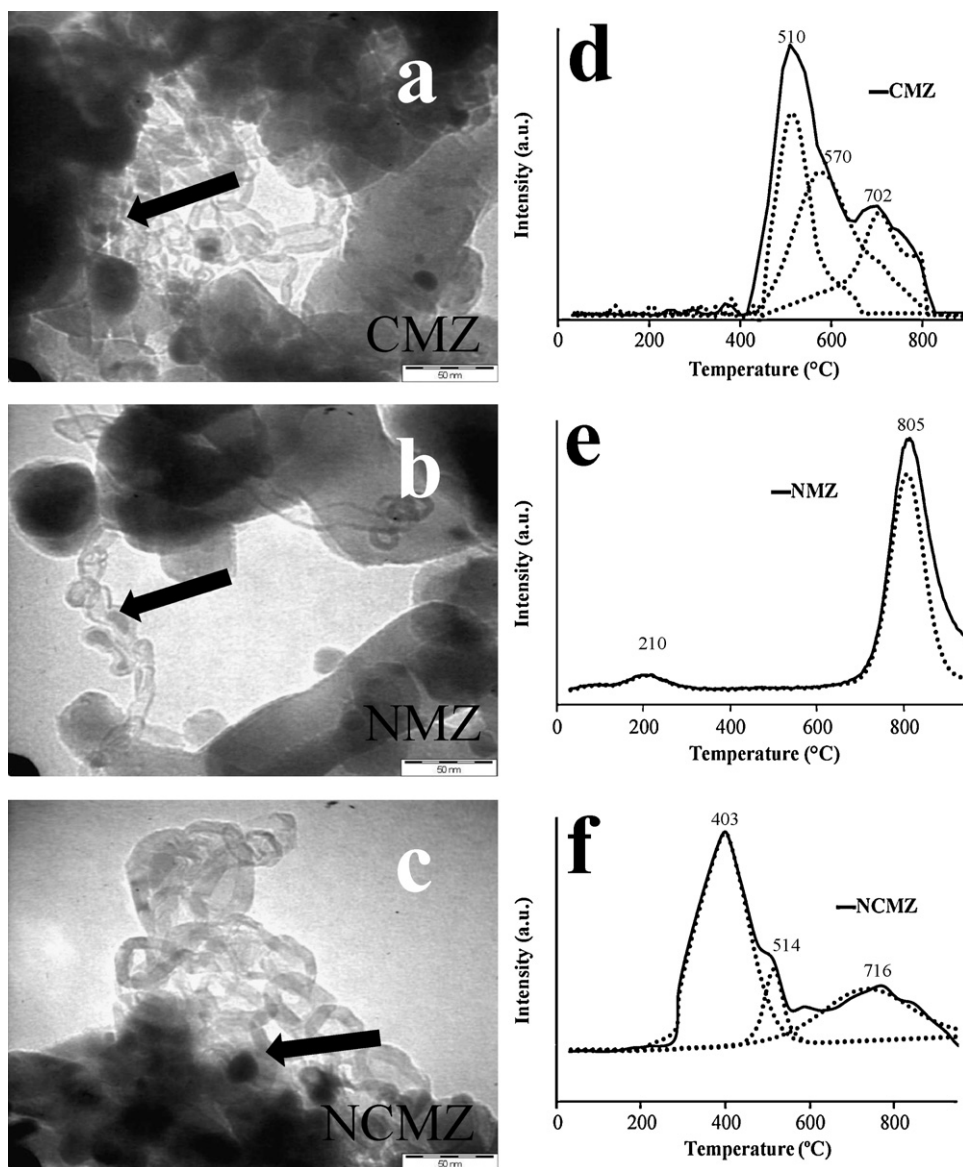


Fig. 9. TEM mapping and TPH profiles for the spent monometallic and bimetallic catalysts.

be due to the encapsulated structure of metal crystallites that limit the contact between metal active sites and reactants.

### 3.7.3. TPH

TPH experiments were conducted to investigate type of coke species deposited on the used catalysts. The findings are presented in Fig. 9d–f for CMZ, NMZ and NCMZ catalysts respectively. Deconvolution of TPH profile identified 3 types of carbonaceous species on the spent CMZ catalyst with different reactivities towards hydrogenation registered at around 510, 570, and 702 °C. The first two peaks, between 300 and 600 °C are defined as  $\alpha$ -carbon and the third one, above 600 °C are assigned as  $\beta$ -carbon which is much less reactive toward hydrogen than  $\alpha$ -carbon [39]. Similar TPH profile also identified for NCMZ catalyst. The first temperature region of carbon deposition is related to amorphous carbon located at the interior of the active metal particles [86] while the second region of coke formation is defined as filamentous whisker carbon where possibly derived from methane decomposition and CO disproportionation [87]. Two hydrogenation peaks were identified for the used NMZ catalyst at around 210 and 805 °C. The first peak is designated to a very reactive carbon species as it located at a

lowest temperature compared to CMZ and NCMZ catalysts. Carbon species located around 805 °C is assigned as  $\gamma$ -carbon [6]. Quek et al. [6] defined the reactivity of carbon species from the most reactive species as follows:  $\alpha$ -carbon >  $\beta$ -carbon >  $\gamma$ -carbon and in term of inertness,  $\gamma$ -carbon would be the hardest carbon species to be removed from the used catalyst. Coke deposition observed in TPH profiles was also consistent with coke deposition data retrieved from TG-DTA analysis (Table 4). As shown in Fig. 8a and b and Table 3, higher activity for both CMZ and NCMZ catalysts than NMZ catalyst. This could be related to formation of  $\alpha$ -carbon and  $\beta$ -carbon which are non-stable carbonaceous species and played a role of reactive intermediate enhancing the catalytic activity. Low activity of NMZ catalyst is attributed to the formation of inert  $\gamma$ -carbon species that were hard to remove during catalytic reaction and led to the possible deactivation.

### 3.7.4. HRTEM

In order to investigate the sintering of active metal, the mean particle size of used catalysts was calculated from the micrograph of HRTEM (Fig. 10). As shown in Table 2, size measurement of 250 particles of the used catalyst by HRTEM imaging revealed that

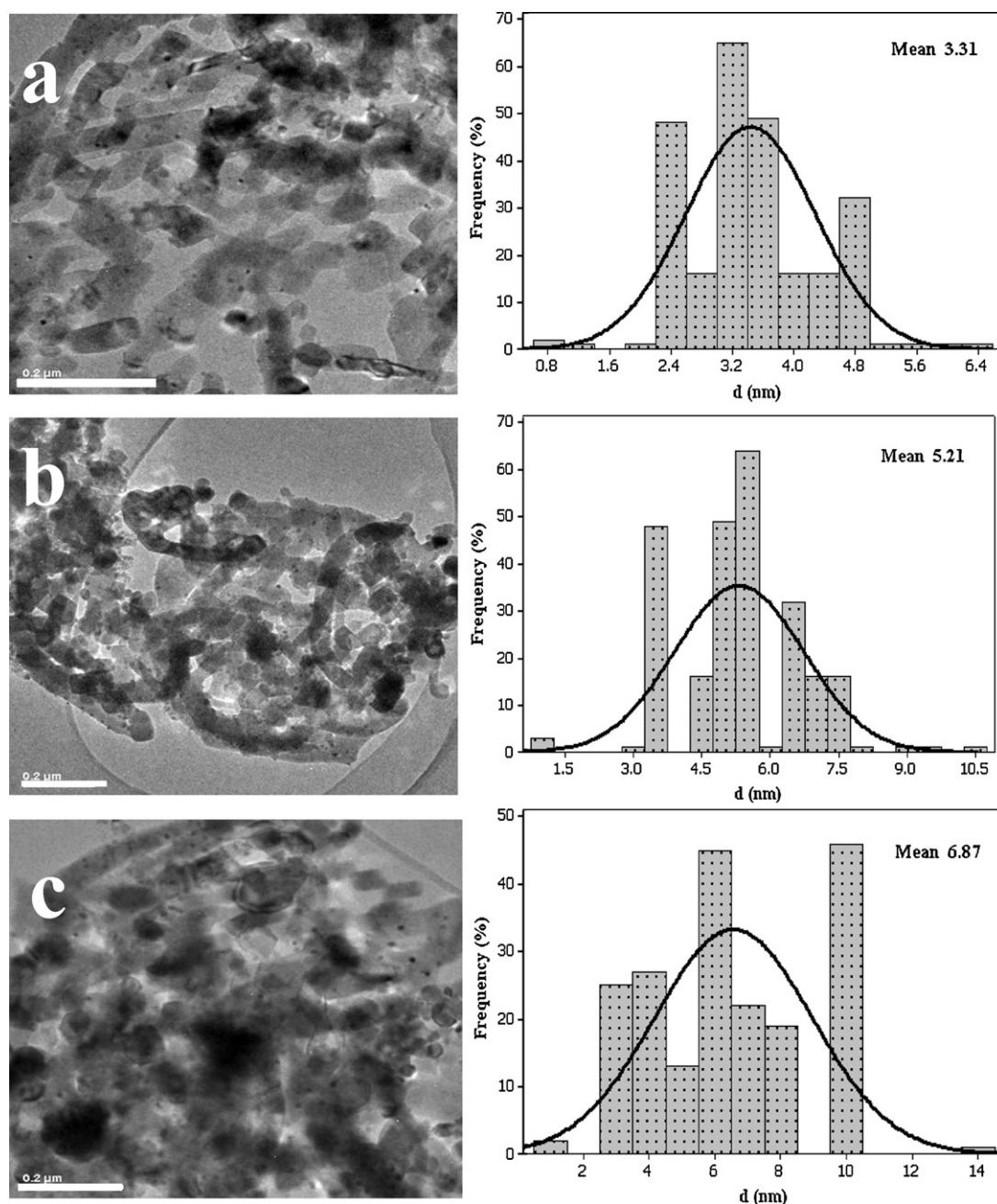


**Fig. 10.** HRTEM images and respective particle size distributions for spent catalysts: (a) used NCMZ, (b) used NMZ and (c) used CMZ.

moderate sintering under reaction condition occurred on all the catalysts samples. CMZ catalyst (Fig. 10c) experienced the largest particle size change with an increment of 9.0% followed by NCMZ catalyst registered 6.8% increase (Fig. 10a) in average particles size compared to fresh catalyst (Fig. 5a). NMZ catalyst (Fig. 10b) experienced the least changes, approximately 4.2% of particle size increment compared to fresh catalyst (Fig. 5b). The largest particles size up to 14 nm was found for CMZ catalyst. Table 4 shows that CMZ catalyst gave the highest rate of coke deposition. This observation was inline with the report from literature [88]. On the other hand, both NCMZ and NMZ catalysts had more homogeneous particle size distribution compared to CMZ catalyst as shown in Fig. 10. NCMZ catalyst has the smallest average particle size but gave higher coke deposition rate compared to NMZ catalyst having larger particle size. This observation was contrary with reported result from literature [89] where carbon deposition was favored metal parti-

cles due to its structure-sensitive nature. The discrepancy of the present work with literature data could be due to the relatively easier decomposition of  $\text{CH}_4$  over small metal particles as experimented by Hou et al. [88] in the pulsed-injection surface reaction of methane. The present result of the coke deposition and particle size also consistent with recent literature reported by Quek et al. research group [6] where smallest particle size catalyst (NCMZ) exhibited good catalytic activity and stability with a relatively large amount of carbonaceous species formed over the catalyst. The formation of coke at the backside of metal crystalline that maintain the accessibility of reactant towards the active sites of the catalyst could contribute to high stability of the catalyst. A number of researchers [15,16,90] reported the relationship between coke formation and metal particle size as can be seen from the analysis of TGA, TEM mapping and HRTEM imaging in Table 4, Figs. 9 and 10, respectively. It has been reported in the literature [15,90] that small metal



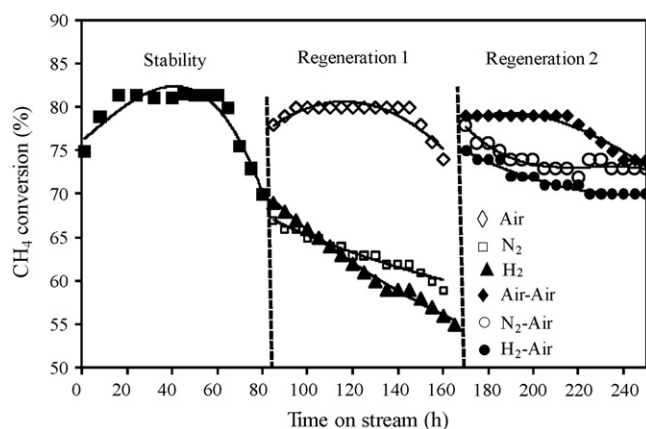


**Fig. 11.** Stability and regenerability study of NCMZ catalyst under various regeneration conditions. Reaction condition:  $T = 750^{\circ}\text{C}$ ,  $P = 1\text{ atm}$ , GHSV = 125,000 ml/g h,  $\text{CH}_4/\text{CO}_2 = 1$ .

particle (smaller than 10 nm) produce carbon filaments with short diameter and favors carbon gasification by carbon dioxide. Generally, the mean particle size of all catalysts as prepared in this work was smaller than 10 nm and filamentous coke with short diameter 15 nm was observed among all catalysts as reported similarly with the literature [15,90].

### 3.8. Long term catalytic study and regenerability of bimetallic catalyst

Fig. 11 shows the stability and regenerability of used catalyst under different regenerating conditions. Bimetallic NCMZ catalyst exhibited similar result as previously discussed where the conversion of methane increased initially and became constant after 8 h in the reaction and the activity started to decline after 60 h of time on stream. The sharp decline in activity could possibly be due to large amount of coke deposited on the catalyst as can be seen in Fig. 12. The reaction system was shut down after 80 h due to pressure buildup in the reactor (coke deposition) before regeneration was initiated. Three sets of stability studies were conducted for further regeneration purpose.

After the stability test, the catalyst was regenerated in-situ in the reactor for 1 h under different regeneration environments including air, nitrogen and hydrogen. The regenerated catalyst was tested under the same reaction conditions as used in the stability test for

the purpose of investigating the influence of different regenerating mediums towards catalytic performance. As shown in Fig. 11, first stage regeneration of deactivated catalyst (Regeneration 1) by air could restore the catalyst performance to  $\approx 80\%$  conversion of methane. On the other hand, nitrogen and hydrogen did not improve the catalytic performance and the activity continued to decrease. These observations also indicated that the catalyst deactivation unlikely to be caused by metal oxidation. Instead, it was mainly due to coke deposition as the effect of air as the regeneration medium was more pronounced than hydrogen gas. This hypothesis was further proven in the second regeneration (Regeneration 2) cycle where all deactivated catalysts from the first regeneration cycle were regenerated with air and the results shown in Fig. 11 as well. For short, air as the regenerating medium could restore almost 100% of catalytic activity of the deactivated catalyst. Thus, bimetallic catalyst in the present work showed constant catalytic activity and used catalyst could be easily regenerated, thus it is a suitable catalyst for catalytic carbon dioxide reforming of methane.

## 4. Conclusion

X-ray diffraction analysis showed the existence of tetragonal phase of zirconia which is active in heterogeneous catalytic system, especially in the present work for carbon dioxide reforming of methane. Besides that, TPR analysis also revealed the synergized effect responsible for lower reduction temperature in bimetallic catalyst. Bimetallic catalyst showed constant catalytic activity after 40 h of continuous reaction operation. Reforming of methane catalyzed by NCMZ catalyst showed that conversion of reactants could be achieved as high as 80% and 84% for  $\text{CH}_4$  and  $\text{CO}_2$  respectively. The constant activity of bimetallic catalyst was explained in terms of high degree of reducibility, synergetic effect between Ni and Co (TPR analysis), inhibition of metal from being oxidized as well as surface basicity to inhibit coke formation (XPS analysis). NCMZ catalyst showed impressive restoration of catalytic activity after used catalyst is regenerated using air. The catalytic activity of used catalyst was restored to achieve comparable catalytic performance as fresh catalyst. The catalytic performance of monometallic nickel and cobalt catalysts was improved through the synergized effect of both components in bimetallic catalyst which showed better activity and regenerability.

## Acknowledgements

The authors gratefully acknowledge the ScienceFund grant (Account no.: 6013335) from the Ministry of Science, Technology and Innovation (MOSTI) of Malaysia and the Research University (RU) grant provided by Universiti Sains Malaysia to support this research work. Special thanks to National Science Fellowship as well for sponsoring one researcher (Mun-Sing Fan).

## References

- [1] T.H. Fleisch, R.A. Sills, *Stud. Surf. Sci. Catal.* 147 (2004) 31–36.
- [2] G.S. Gallego, C. Batiot-Dupeyrat, J. Barraut, F. Mondragón, *Ind. Eng. Chem. Res.* 47 (2008) 9272–9278.
- [3] J.R.H. Ross, *Catal. Today* 100 (2005) 151–158.
- [4] Z. Jiang, T. Xiao, V.L. Kuznetsov, P.P. Edwards, *Philos. Trans. R. Soc. Lond. Ser. A* 368 (2010) 3343–3364.
- [5] T.V. Choudhary, V.R. Choudhary, *Angew. Chem. Int. Ed.* 47 (2008) 1828–1847.
- [6] X.-Y. Quek, D. Liu, W.N.E. Cheo, H. Wang, Y. Chen, Y. Yang, *Appl. Catal. B* 95 (2010) 374–382.
- [7] P. Dokamaingam, N. Laosiripojana, A. Soottitawat, S. Assabumrungrat, *AIChE J.* 56 (2010) 1639–1650.
- [8] S. Assabumrungrat, S. Charoenseri, N. Laosiripojana, W. Kiatkittipong, P. Praserttham, *Int. J. Hydrogen Energy* 34 (2009) 6211–6220.
- [9] J. Xu, W. Zhou, Z. Li, J. Wang, J. Ma, *Int. J. Hydrogen Energy* 34 (2009) 6646–6654.
- [10] A.E. Castro Luna, M. Iriarte, *Appl. Catal. A* 343 (2008) 10–15.

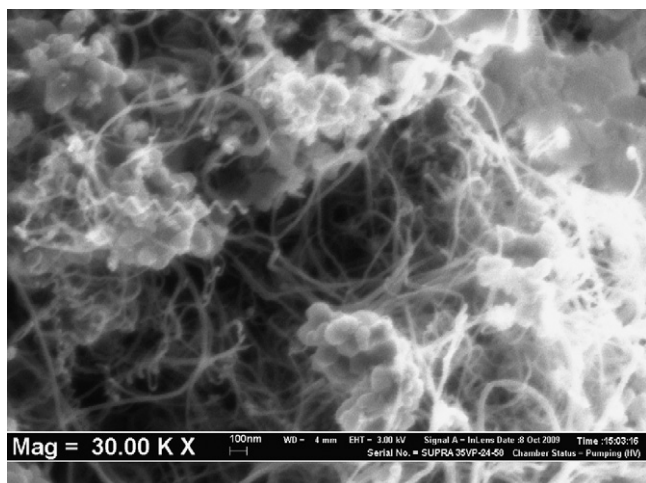


**Fig. 12.** SEM image of the spent catalyst after long term catalytic reaction.



- [11] F. Barrai, T. Jackson, N. Whitmore, M.J. Castaldi, *Catal. Today* 129 (2007) 391–396.
- [12] Y.H. Hu, E. Ruckenstein, C.G. Bruce, K. Helmut, *Advance Catalysis*, Academic Press, 2004, pp. 297–345.
- [13] D. Liu, X.Y. Quek, W.N.E. Cheo, R. Lau, A. Borgna, Y. Yang, *J. Catal.* 266 (2009) 380–390.
- [14] J. Zhang, H. Wang, A.K. Dalai, *J. Catal.* 249 (2007) 300–310.
- [15] D. San-José-Alonso, J. Juan-Juan, M.J. Illán-Gómez, M.C. Román-Martínez, *Appl. Catal. A* 371 (2009) 54–59.
- [16] J. Zhang, H. Wang, A.K. Dalai, *Appl. Catal. A* 339 (2008) 121–129.
- [17] Z. Zhang, X.E. Verykios, *Appl. Catal. A* 138 (1996) 109–133.
- [18] M. Rezaei, S.M. Alavi, S. Sahebdehfar, Z.-F. Yan, *Energy Fuels* 22 (2008) 2195–2202.
- [19] B. Matas Güell, I.M.T.d. Silva, K. Seshan, L. Lefferts, *Appl. Catal. B* 88 (2009) 59–65.
- [20] N. Tangchupong, W. Khaoee, B. Jongsomjit, N. Laosiripojana, P. Praserttham, S. Assabumrungrat, *Fuel Process. Technol.* 91 (2010) 121–126.
- [21] P.D.L. Mercera, J.G. van Ommen, E.B.M. Doesburg, A.J. Burggraaf, J.R.H. Roes, *Appl. Catal.* 78 (1991) 79–96.
- [22] J. Goscińska, M. Ziolk, E. Gibson, M. Daturi, *Appl. Catal. B* 97 (2010) 49–56.
- [23] T. Yasu-eda, S. Kitamura, N.-o. Ikenaga, T. Miyake, T. Suzuki, *J. Mol. Catal. A Chem.* 323 (2010) 7–15.
- [24] K. Tanabe, *Mater. Chem. Phys.* 13 (1985) 347–364.
- [25] E.O. Bensadon, P.A.P. Nascente, P. Olivi, L.O.S. Bulhões, E.C. Pereira, *Chem. Mater.* 11 (1998) 277–280.
- [26] J.D.A. Bellido, E.M. Assaf, *Appl. Catal. A* 352 (2009) 179–187.
- [27] M. Rezaei, S.M. Alavi, S. Sahebdehfar, Z.-F. Yan, *Mater. Lett.* 61 (2007) 2628–2631.
- [28] R. Muccillo, R.C. Buissa Netto, E.N.S. Muccillo, *Mater. Lett.* 49 (2001) 197–201.
- [29] K. Nakamura, T. Miyazawa, T. Sakurai, T. Miyao, S. Naito, N. Begum, K. Kunimori, K. Tomishige, *Appl. Catal. B* 86 (2009) 36–44.
- [30] J. Liu, H. Hu, L. Jin, P. Wang, S. Zhu, *Fuel Process. Technol.* 91 (2010) 419–423.
- [31] Z. Yang, Y. Zhang, X. Wang, X. Lu, W. Ding, *Energy Fuels* 24 (2010) 785–788.
- [32] W. Hua, L. Jin, X. He, J. Liu, H. Hu, *Catal. Commun.* 11 (2010) 968–972.
- [33] D. Gulková, O. Šolcová, M. Zdražil, *Microporous Mesoporous Mater.* 76 (2004) 137–149.
- [34] X. Li, J.-S. Chang, M. Tian, S.-E. Park, *Appl. Organomet. Chem.* 15 (2001) 109–112.
- [35] V. García, J.J. Fernández, W. Ruiz, F. Mondragón, A. Moreno, *Catal. Commun.* 11 (2009) 240–246.
- [36] F. Meshkani, M. Rezaei, *Powder Technol.* 196 (2009) 85–88.
- [37] P.A. Webb, C. Orr, R.W. Camp, J.P. Oliver, Y.S. Yunes, *Analytical Method in Fine Particle Technology*, first ed., Micromeritics, 1997.
- [38] L. He, H. Berntsen, E. Ochoa-Fernández, J. Walmsley, E. Blekkan, D. Chen, *Top. Catal.* 52 (2009) 206–217.
- [39] A. Becerra, M. Dimitrijewits, C. Arciprete, A. Castro Luna, *Granular Matter* 3 (2001) 79–81.
- [40] M. Rezaei, S.M. Alavi, S. Sahebdehfar, Z.-F. Yan, *J. Nat. Gas Chem.* 17 (2008) 278–282.
- [41] N. Laosiripojana, S. Assabumrungrat, *Appl. Catal. B* 60 (2005) 107–116.
- [42] Y.T. Chua, A.R. Mohamed, S. Bhatia, *Appl. Catal. A* 343 (2008) 142–148.
- [43] W. Córdova-Martínez, E. De la Rosa-Cruz, L.A. Díaz-Torres, P. Salas, A. Montoya, M. Avendaño, R.A. Rodríguez, O. Barbosa-García, *Opt. Mater.* 20 (2002) 263–271.
- [44] H. Teterycz, R. Klimkiewicz, M. Laniecki, *Appl. Catal. A* 249 (2003) 313–326.
- [45] G. Centi, G. Cerrato, S. D'Angelo, U. Finardi, E. Giamello, C. Morterra, S. Perathoner, *Catal. Today* 27 (1996) 265–270.
- [46] T. Yamaguchi, *Catal. Today* 20 (1994) 199–217.
- [47] J.G. Jakobsen, T.L. Jørgensen, I. Chorkendorff, J. Sehested, *Appl. Catal. A* 377 (2010) 158–166.
- [48] J.A. Montoya, E. Romero, A. Monzón, C. Guimon, *Stud. Surf. Sci. Catal.* 130 D (2000) 3669–3674.
- [49] M. Rezaei, S.M. Alavi, S. Sahebdehfar, P. Bai, X. Liu, Z.-F. Yan, *Appl. Catal. B* 77 (2008) 346–354.
- [50] K. Petrov, G. Will, *J. Mater. Sci. Lett.* 6 (1987) 1153–1155.
- [51] PDF-2 Joint Committee on Powder Diffraction Standards, International Center of Diffraction Data, Park Lane Swarthmore, Pennsylvania, USA, 1994.
- [52] C.M. Woodbridge, C.B. Frech, *J. Chem. Educ.* 87 (2010) 272–274.
- [53] K.W. Kolasinski, *Surface Science: Foundations of Catalysis and Nanoscience*, second ed., 2008.
- [54] K.S.W. Sing, *J. Porous Mater.* 2 (1995) 5–8.
- [55] H. Marsh, F. Rodríguez-Reinoso, *Activated Carbon*, Elsevier, 2006.
- [56] N. Sun, X. Wen, F. Wang, W. Wei, Y. Sun, *Energy Environ. Sci.* 3 (2010) 366–369.
- [57] P.I. Ravikovitch, A.V. Neimark, *Langmuir* 18 (2002) 9830–9837.
- [58] S. Liu, X. Zhang, J. Li, N. Zhao, W. Wei, Y. Sun, *Catal. Commun.* 9 (2008) 1527–1532.
- [59] M.A. Vannice, *Kinetics of Catalytic Reactions*, Springer, New York, 2005, pp. 1–257.
- [60] C.C. Yu, S.T. Oyama, *J. Mater. Sci.* 30 (1995) 4037–4042.
- [61] G. Zhang, M.M. Habib, S.E. Vittoratos, *J. Phys. IV* 7 (1997).
- [62] R.G. Ding, Z.F. Yan, Adsorption properties studies of the nickel catalysts for carbon dioxide reforming of methane, ACS Division of Fuel Chemistry, Preprints, 1 ed., Orlando, FL, 2002, pp. 103–105.
- [63] G. Jacobs, J.A. Chaney, P.M. Patterson, T.K. Das, B.H. Davis, *Appl. Catal. A* 264 (2004) 203–212.
- [64] E.B. Pereira, N. Homs, S. Martí, J.L.G. Fierro, P. Ramírez de la Piscina, *J. Catal.* 257 (2008) 206–214.
- [65] V.G. Milt, M.A. Ulla, E.A. Lombardo, *Catal. Lett.* 65 (2000) 67–73.
- [66] K.C. Mondal, V.R. Choudhary, U.A. Joshi, *Appl. Catal. A* 316 (2007) 47–52.
- [67] N. Luo, K. Ouyang, F. Cao, T. Xiao, *Biomass Bioenergy* 34 (2010) 489–495.
- [68] T. Furusawa, A. Tsutsumi, *Appl. Catal. A* 278 (2005) 207–212.
- [69] H. Tanaka, R. Kaino, K. Okumura, T. Kizuka, Y. Nakagawa, K. Tomishige, *Appl. Catal. A* 378 (2010) 175–186.
- [70] T. Kuznetsova, V. Sadykov, *Kinet. Catal.* 49 (2008) 840–858.
- [71] J. Chen, Q. Wu, J. Zhang, J. Zhang, *Fuel* 87 (2008) 2901–2907.
- [72] K. Takanabe, K. Nagaoka, K. Nariai, K.-i. Aika, *J. Catal.* 232 (2005) 268–275.
- [73] R. Xu, H.C. Zeng, *Chem. Mater.* 15 (2003) 2040–2048.
- [74] Q. Yang, H. Choi, D.D. Dionysiou, *Appl. Catal. B* 74 (2007) 170–178.
- [75] W. Zhang, H.L. Tay, S.S. Lim, Y. Wang, Z. Zhong, R. Xu, *Appl. Catal. B* 95 (2010) 93–99.
- [76] P.K. Cheekatamarla, A.M. Lane, *Int. J. Hydrogen Energy* 30 (2005) 1277–1285.
- [77] J.M. Rynkowski, T. Paryczak, M. Lenik, M. Farbotko, J. Góralski, *J. Chem. Soc. Faraday Trans.* 91 (1995) 3481–3484.
- [78] O. Cairon, E. Dumitriu, C. Guimon, *J. Phys. Chem. C* 111 (2007) 8015–8023.
- [79] K.V.R. Chary, G.V. Sagar, C.S. Srikanth, V.V. Rao, *J. Phys. Chem. B* 111 (2006) 543–550.
- [80] M.C.J. Bradford, M.A. Vannice, *Catal. Rev. Sci. Eng.* 41 (1999) 1–42.
- [81] M.-S. Fan, A.Z. Abdullah, S. Bhatia, *ChemCatChem* 1 (2009) 192–208.
- [82] V.R. Choudhary, A.S. Mamman, *J. Chem. Technol. Biotechnol.* 73 (1998) 345–350.
- [83] E. Ruckenstein, Y.H. Hu, *Ind. Eng. Chem. Res.* 37 (1998) 1744–1747.
- [84] Z. Hao, Q. Zhu, Z. Jiang, B. Hou, H. Li, *Fuel Process. Technol.* 90 (2009) 113–121.
- [85] Y. Liu, Z. Xu, T. Cheng, G. Zhou, J. Wang, W. Li, Y. Bi, K. Zhen, *Kinet. Catal.* 43 (2002) 522–527.
- [86] E.B. Pereira, G.-A. Martin, *Appl. Catal. A* 115 (1994) 135–146.
- [87] M. Rezaei, S.M. Alavi, S. Sahebdehfar, Z.-F. Yan, *J. Nat. Gas Chem.* 15 (2006) 327–334.
- [88] Z. Hou, J. Gao, J. Guo, D. Liang, H. Lou, X. Zheng, *J. Catal.* 250 (2007) 331–341.
- [89] J.-H. Kim, D.J. Suh, T.-J. Park, K.-L. Kim, *Appl. Catal. A* 197 (2000) 191–200.
- [90] J. Juan-Juan, M.C. Román-Martínez, M.J. Illán-Gómez, *Appl. Catal. A* 355 (2009) 27–32.